

# Spontaneous Generated Convective Anticyclones in Low Latitude — A Model for the Great Red Spot

Tao Cai (✉ [tcai@must.edu.mo](mailto:tcai@must.edu.mo))

Macau University of Science and Technology <https://orcid.org/0000-0003-3431-8570>

Kwing L. Chan

Macau University of Science and Technology <https://orcid.org/0000-0002-6428-1812>

Kim-Chiu Chow

Macau University of Science and Technology

---

## Article

**Keywords:** convection, Great Red Spot, Joivan atmosphere, vortices, rotation

**Posted Date:** June 22nd, 2021

**DOI:** <https://doi.org/10.21203/rs.3.rs-351661/v1>

**License:** © ⓘ This work is licensed under a Creative Commons Attribution 4.0 International License.

[Read Full License](#)

---

# Spontaneous Generated Convective Anticyclones in Low Latitude — A Model for the Great Red Spot

Tao Cai<sup>a,\*</sup>, Kwing L. Chan<sup>a</sup>, Kim-Chiu Chow<sup>a</sup>

<sup>a</sup>*State Key Laboratory of Lunar and Planetary Sciences, Macau University of Science and Technology,  
Macau, People's Republic of China*

---

## Abstract

The Great Red Spot at about latitude  $22^\circ S$  of Jupiter has been observed for hundreds of years, yet the driving mechanism on the formation of this giant anticyclone still remains unclear. Two scenarios were proposed to explain its formation. One is a shallow model suggesting that it might be a weather feature formed through a merging process of small shallow storms generated by moist convection, while the other is a deep model suggesting that it might be a deeply rooted anticyclone powered by the internal heat of Jupiter. In this work, we present numerical simulations showing that the Great Red Spot could be naturally generated in a deep rotating turbulent flow and survive for a long time, when the convective Rossby number is smaller than a certain critical value. From this critical value, we predict that the Great Red Spot extends at least about 500 kilometers deep into the Jovian atmosphere. Our results demonstrate that the Great Red Spot is likely to be a feature deep-seated in the Jovian atmosphere.

*Keywords:*

convection, Great Red Spot, Jovian atmosphere, vortices, rotation

---

## 1. Introduction

Vortices are ubiquitous in gas giant planets. In Jupiter, more than 500 vortices have been identified from the sequence of 70-day Cassini images with latitude spanning from  $80^\circ S$  to  $80^\circ N$  (Li et al., 2004). Recent observation from the Juno spacecraft has detected multiple closely-packed cyclones in the northern and southern polar regions (Adriani et al., 2018; Tabataba-Vakili et al., 2020). Anticyclones of sizes larger than 1000km were also observed in the polar regions of Jupiter, among which most were found to form a dipole configuration with a cyclone (Adriani et al., 2020). The Great Red Spot (GRS), is probably the most prominent large-scale vortex in Jupiter, which is an anticyclone centered at about  $22^\circ S$  and has been observed for hundreds of years. The origin of GRS, however, remains a puzzle.

To understand the origin and existence of large-scale vortices (LSVs) in Jupiter, two scenarios of flow dynamics have been proposed based on different assumptions on the depth of the Jovian atmosphere. The first is a shallow model in which jets (Liu & Schneider, 2010; Lian & Showman, 2010) and vortices (Zhang & Showman, 2014; O'Neill et al., 2015) are

---

\*tcai@must.edu.mo

15 driven by the energy generated from the latent heat of moist convection. The second is a  
16 deep model in which columnar jets (Bussse, 1976; Christensen, 2001; Heimpel & Aurnou,  
17 2007; Cai & Chan, 2012; Aurnou et al., 2015) and vortices (Chan & Mayr, 2013; Heimpel et  
18 al., 2016; Cai et al., 2021) are maintained by the energy deep from the interior of Jupiter.

19 While the depth of the Jovian atmosphere is uncertain, recent measurement on gravity  
20 field by Juno indicates that the zonal jets could possibly extend thousands of kilometers deep  
21 into the atmosphere (Kaspi et al., 2018; Guillot et al., 2018). The heating of Jupiter’s upper  
22 atmosphere also reveals that the GRS should be heated from below, suggesting that it might  
23 have a deep origin (O’Donogue et al., 2016). Although there are some evidences favoring  
24 the deep model, it is fair to say that the possibility of the shallow scenario is not entirely  
25 excluded (Kong et al., 2018).

26 Even if one assumes that the atmosphere is deep, it is natural to ask whether LSVs,  
27 such as GRS could be formed. Previous simulations on rotating compressible convection  
28 (Chan, 2007; Käpylä et al., 2011) revealed that LSVs could be generated in a rapidly rotating  
29 turbulent flow. Later, the dynamics of LSVs has been intensively studied in a rapidly rotating  
30 Rayleigh-Bénard convection (Guervilly et al., 2014; Rubio et al., 2014; Favier et al., 2014).  
31 Despite the considerable progress achieved in these simulations, there are some limitations  
32 in these studies. First, the heat fluxes used in these simulations (Chan, 2007; Käpylä et al.,  
33 2011) are larger than Jupiter’s internal heat flux by several magnitudes. Second, in previous  
34 simulations on rapidly rotating convection only shear (Novi et al., 2019; Currie & Tobias,  
35 2020) or large-scale cyclones (Chan & Mayr, 2013) can be found in low latitudes. The present  
36 study is motivated by the following questions. Could LSVs be generated in deep convective  
37 flow with a flux at or close to Jupiter’s internal heat? Could large-scale anticyclones, such  
38 as GRS, be generated in a rapidly rotating turbulent flow at low latitudes? Results of some  
39 numerical simulations will be discussed in the following sections to address these questions.

## 40 2. Result

### 41 2.1. How to generate LSVs at Jupiter-like small flux?

42 We first consider the simulations of rotating turbulent convection in a  $f$ -plane at high  
43 latitudes. The computational domain is a Cartesian box with a constant flux fed at the  
44 bottom. The simulations were performed with a semi-implicit mixed finite-difference spectral  
45 code (Cai, 2016), which accounts for the effects of density stratification, compressibility, and  
46 subgrid scale turbulence (see Appendix A). We use dimensionless variables in the code, with  
47 all the variables normalized by the values of height, pressure, density, and temperature at  
48 the top of the box. For example, the velocity is normalized by  $(p_{top}/\rho_{top})^{1/2}$ , and the flux is  
49 normalized by  $\rho_{top}(p_{top}/\rho_{top})^{3/2}$ , where  $p_{top}$  and  $\rho_{top}$  are the pressure and density at the top  
50 of box, respectively. The box has an aspect ratio of  $\Gamma = 4$  (lateral dimension to height),  
51 and a resolution of  $512^2 \times 101$  grid points. We simulate a deep flow with a total depth of  
52 about 3.2 pressure scale height at latitude  $\theta = 90^\circ$ , with the dimensionless rotation rate  $\Omega$   
53 spanning from 0 to 5.12, and the dimensionless total flux  $F_{tot}$  spanning from  $10^{-5}$  to  $10^{-2}$ .  
54 Additional parameters of the simulation cases are given in Table S1 (see Appendix D). The  
55 initial thermal structure of each simulation is a polytrope, with about 80 percent of the total  
56 flux  $F_{tot}$  carried by radiation or conduction, and the rest 20 percent is carried by convection  
57 when convection is well developed (convective flux  $F_c \sim 0.2F_{tot}$ ). In Jupiter, almost all the

58 flux is transported by convection. Here we raise the proportion of flux carried by radiation  
 59 or conduction to keep the Prandtl number small and speed up the thermal relaxation. This  
 60 technique has been widely used in simulations of stellar and planetary convection (Brummel  
 61 et al., 2002; Rogers & Glatzmaier, 2005; Cai, 2020; Cai et al., 2021).

62 After a small initial perturbation and a long period of evolution (at least several thermal  
 63 relaxation time  $\tau_{th} \sim 1/F_{tot}$ ), the convective flow reaches a statistically thermal equilibrium  
 64 state. Two transitions in flow patterns take place as the rotation rate increases (Fig. 1). The  
 65 convective Rossby number  $Ro_c (= \langle v'' \rangle_{ref} / (2\Omega H)$ , where  $\langle v'' \rangle_{ref}$  is the averaged root-mean-  
 66 square convective velocity, calculated at an independent non-rotating reference case;  $H$  is the  
 67 height of the box; and  $\Omega$  is the rotation rate), which measures the importance of buoyancy  
 68 to rotational effects (see Appendix B), is an essential parameter to control the transitions  
 69 of flow patterns (Chan & Mayr, 2013; Guervilly et al., 2014).

70 The first transition from turbulence (regime I) to large-scale cyclones (regime II, the flow  
 71 is still turbulent but large-scale cyclones appear) occurs when  $Ro_c$  is smaller than a critical  
 72 number  $Ro_{c1} \sim 0.11$  (Fig. 2A). It is followed by a second transition to the appearance of  
 73 large-scale anticyclones (regime III, the flow is still turbulent but large-scale anticyclones  
 74 appear) when  $Ro_c$  further decreases to another critical number  $Ro_{c2} \sim 0.023$  (Fig. 2A). This  
 75 result is insensitive to various parameters, such as the magnitude of flux, the Prandtl number,  
 76 and the Ekman number, at least in the parameter space that has been explored. The large-  
 77 scale cyclones and anticyclones can survive for a long time. For example, the vortices in Case  
 78 D7 are still alive after 1600 rotation periods. In regime II, a pair of cyclones in Case A4  
 79 have survived for at least 100 rotation periods. It indicates that multiple cyclones could be  
 80 generated in a deep rotating convection zone. When curvature effect is taken into account,  
 81 these multiple cyclones tend to cluster around the pole (Cai et al., 2021), which may explain  
 82 the driving mechanics of the circumpolar cyclones observed in Jupiter’s poles (Adriani et al.,  
 83 2018, 2020). In regime III, counter rotating vortex dipoles are formed in most cases, similar to  
 84 the dipole configurations observed in the Jupiter’s southern polar region ( $10^\circ$  away from the  
 85 pole) (Adriani et al., 2020). Mach number also has effect on the survivorship of cyclones. Case  
 86 A6 shows that a cyclone (Fig. 1) is twisted and almost destructed when the Mach number  
 87 reaches one. Similar phenomenon is observed in Case A7. In other cases, cyclones are stable  
 88 since their speeds are subsonic. Mach number decreases with the convective flux (Table S1).  
 89 The vertical velocity is much smaller than the horizontal velocity in rapidly rotating flow  
 90 (Fig. 2C and D), thus the Mach number reflects the maximum wind speed of the LSVs. As  
 91 the convective flux of Jupiter is lower, we expect that the LSVs in Jupiter are subsonic. The  
 92 horizontal velocity reaches a peak value near the second transition state when the large-scale  
 93 anticyclones appear (Fig. 2C). Passing through this transition state, the horizontal velocity  
 94 and vortex size decrease with decreasing  $Ro_c$ . The observed decreasing vortex size with  
 95 decreasing  $Ro_c$  is in agreement with the theoretical analysis of Coriolis-Inertial-Archimedean  
 96 (CIA) balance on rapidly rotating convection (Christensen, 2010), from which the relative  
 97 size of LSVs at small  $Ro_c$  obeys a scaling  $\ell/h \sim Ro_c^{1/2}$ , where  $\ell$  and  $h$  are horizontal and  
 98 vertical length scales of a vortex respectively (see Appendix B).

99 Now we can apply the simulation result to Jupiter. The pressure and density at Jupiter’s  
 100 surface are  $10^5 \text{Pa}$  and  $0.167 \text{kg/m}^3$  respectively. The internal heat flux of Jupiter is estimated  
 101 to be  $7.48 \text{Wm}^{-2}$  (Li et al., 2018). For Jupiter, the dimensionless total flux  $F_{tot,J}$  is about  
 102  $1 \times 10^{-7}$ , which is almost carried by convection. The convective flux  $F_c$  calculated in the

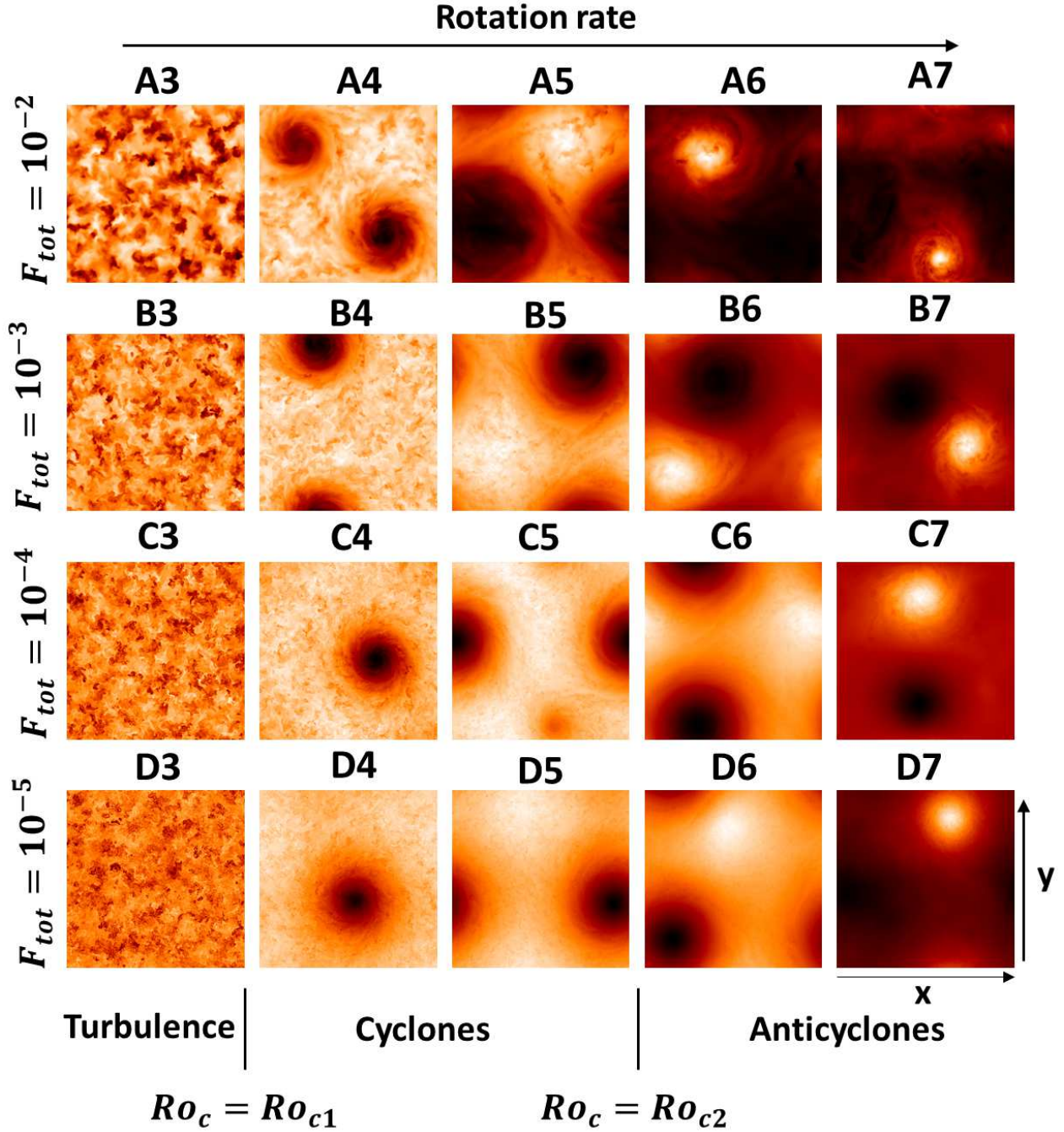


Figure 1: Flow patterns for rotating convection at the high latitude  $\theta = 90^\circ$ . Snapshots of the temperature perturbation taken horizontally at the mid of the convection zone  $z = 0.5$ . The bright (dark) color denotes higher (lower) temperature. From top to bottom, the panels show four groups with different total fluxes  $F_{tot} \in \{10^{-2}, 10^{-3}, 10^{-4}, 10^{-5}\}$ , respectively. The subtitle of each small figure shows the specific case number. Flow patterns are separated into three regimes by  $Ro_{c1}$  and  $Ro_{c2}$ : the turbulence, the large-scale cyclones, and the large-scale anticyclones.

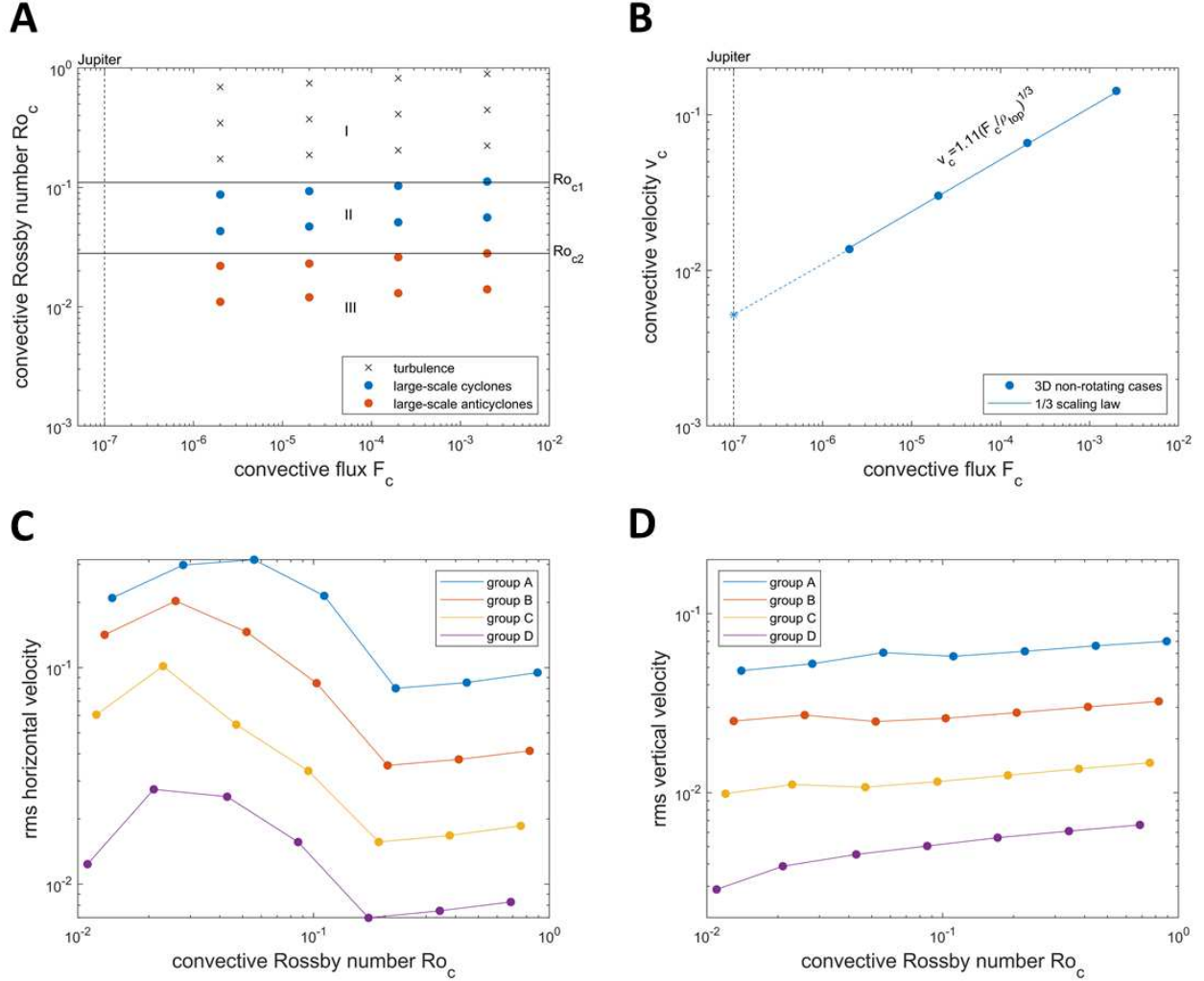


Figure 2: Results of rotating flow at high latitudes. (A) Transitions of flow patterns in rapidly rotating convection. The computed cases are shown in the  $F_c - Ro_c$  diagram. The symbols cross, blue cycle, and red cycle denote turbulence, large-scale cyclones, and the large-scale anticyclones, respectively. These three regimes I, II, and III are separated by  $Ro_{c1}$  and  $Ro_{c2}$ . The vertical dashed line shows the location of Jupiter’s convective flux in the diagram. (B) Scaling of convective velocity. The convective velocity  $v_c$  as a function of the convective flux  $F_c$  for the non-rotating Cases A0, B0, C0, and D0. The root-mean-square velocity  $\langle v'' \rangle$  is used as  $v_c$ .  $\rho_{top}$  is the density at the top of the box. (C) and (D) are the time averaged root-mean-square horizontal and vertical velocities, respectively. Groups A-D represent four groups with different total fluxes  $F_{tot} \in \{10^{-2}, 10^{-3}, 10^{-4}, 10^{-5}\}$ .

103 simulation group D ( $F_c \sim 2 \times 10^{-6}$ ) is close to the realistic values in gas giant planets (for  
 104 Jupiter,  $F_{c,J} \sim 1 \times 10^{-7}$ ). Our simulation has shown that the essential factor on determining  
 105 the appearance of LSVs is the convective Rossby number  $Ro_c$ . It leads to the argument that  
 106 this result could be extrapolated to the Jovian atmosphere. To obtain  $Ro_c$  in Jupiter, we first  
 107 make an estimation on the convective velocity  $\langle v'' \rangle$  of a non-rotating Jupiter. From the mixing  
 108 length theory,  $\langle v'' \rangle$  has a scaling relation with the convective velocity  $F_c$  of  $\langle v'' \rangle \sim (F_c/\rho)^{1/3}$   
 109 (Böhm-Vitense, 1958; Chan & Sofia, 1989), where  $\rho$  is density. The 1/3 scaling law is tested  
 110 against the data of the non-rotating cases (Fig.2B). The data shows a scaling relation  $\langle v'' \rangle =$   
 111  $1.11(F_c/\rho_{top})^{1/3}$ , which is remarkably consistent with the theoretical mixing-length prediction.  
 112 With this scaling relation, the dimensionless convective velocity of a non-rotating Jupiter is  
 113 predicted to be 0.0052, which corresponds to 4.02m/s. As the angular velocity of Jupiter is a  
 114 constant  $1.76 \times 10^{-4}$ rad/s, the appearances of large-scale cyclones or anticyclones in Jupiter  
 115 solely depend on the depth of atmosphere  $H$ . For a given  $Ro_{c1}$  or  $Ro_{c2}$ , the lower limit of  
 116  $H$  can be inferred. Recently, large-scale cyclones and anticyclones have been observed on  
 117 Jupiter's poles by the Juno spacecraft (Adriani et al., 2018, 2020). The condition for the  
 118 emergence of LSVs can be applied to the poles. To satisfy  $Ro_c \leq Ro_{c1}$ , we expect that the  
 119 depth of Jovian atmosphere is deeper than  $H_{c1} = \langle v'' \rangle_{ref} / (2\Omega Ro_{c1}) \approx 102$ km in the polar  
 120 region. To generate anticyclone in the polar region, it is expected that the Jovian atmosphere  
 121 is deeper than  $H_{c2} = \langle v'' \rangle_{ref} / (2\Omega Ro_{c2}) \approx 501$ km. As both cyclones and anticyclones exist,  
 122 we predict that Jupiter's atmosphere is at least 500km deep in the polar regions. Juno's  
 123 gravitational measurement predicted that the depth of atmosphere at polar regions is in the  
 124 range of  $0 \sim 500$ km (Kaspi et al., 2018). The lower limit of our prediction coincides with the  
 125 upper limit of the prediction from gravitational measurement.

## 126 2.2. How to generate GRS-like LSVs in low latitudes?

127 We have shown that LSVs can be generated in a rapidly rotating deep convective flow at  
 128 high latitudes. Now we demonstrate by simulations that LSVs can also survive in a rotating  
 129 flow at low latitudes. For simulation parameters at low latitudes,  $\theta$  is fixed at  $22.5^\circ$ ,  $F_{tot}$   
 130 is from  $10^{-5}$  to  $10^{-3}$ , and  $\Omega$  is from 0.16 to 2.56 (see Table S2 in Appendix D). The  
 131 basic settings are almost the same as the simulations at high latitudes, except that now the  
 132 rotational axis is inclined with gravitational axis by an angle  $67.5^\circ$ .

133 The appearances of LSVs in rapidly rotating flow at low latitudes are shown in Fig. 3.  
 134 Also apparent is that large scale anticyclone, similar to GRS observed at Jupiter's low lat-  
 135 itude, are formed when  $Ro_c$  is small. In simulations at high latitudes, columnar circular  
 136 vortices are aligned with the rotational axis. Unlike previous simulations, here we see that  
 137 the axially aligned columnar vortices are elliptic rather than circular (Fig. 4A). This can  
 138 be made more clear by illustrating the flow structure at a cut plane perpendicular to  $\Omega$   
 139 (Fig. 4E). It demonstrates that elliptic vortex could be generated in deep convective rotating  
 140 flow. The flow patterns on the meridional-zonal ( $x-y$ ), zonal-vertical ( $x-z$ ), and meridional-  
 141 vertical ( $y-z$ ) planes can be viewed as the projections of the elliptic vortex. Interestingly, the  
 142 large-scale anticyclone on the  $x-y$  plane shows a circular structure (Fig. 4B), while on the  
 143  $x-z$  plane it remains elliptic (Fig. 4C). This suggests that the vertical component of angular  
 144 velocity ( $\Omega \sin \theta \hat{z}$ ) plays a leading role in the formation of LSVs. Recently, observation has  
 145 shown that the GRS is changing from elliptical shape to circular shape, which shares some  
 146 similarity with our simulation result. Tilted patterns, which are parallel to  $\Omega$  as exhibited

147 on the  $y$ - $z$  plane (Fig.4D), demonstrating that the columnar structure is indeed aligned with  
 148  $\Omega$ . The LSVs are stable for a very long time. For example, the vortices in Case D7b have  
 149 survived for at least 400 rotating periods till we terminate the simulation. Movies S1, S2, S3  
 150 and S4 (see Appendix F) show the flow motions at different planes  $z = 0.1$ ,  $z = 0.9$ ,  $y = 3.6$ ,  
 151 and  $x = 3.6$  for about 27 rotating periods. In movies S1 (horizontal plane cut at  $z=0.1$ )  
 152 and S2 (at  $z=0.9$ ), small scale turbulent motions are observed inside the anticyclone, similar  
 153 to the fluid motions observed in Juno image (Sánchez-Lavega et al., 2018). The large-scale  
 154 anticyclone can be better understood by showing vortical structures. Surprisingly, only small  
 155 vortical tubes (SVTs) (aligned with  $\Omega$ ) are observed in the instantaneous vortical structure  
 156 (Fig.4F). Tube-like vortices were found associated with strong down flows in deep convection  
 157 (Brummel et al., 2002). Movie S5 on vortical structure indicates that LSVs are actually  
 158 formed by the organized movements of these SVTs. The formation of LSVs are mainly con-  
 159 tributed by the asymmetry distribution of positive and negative SVTs. The positive SVTs  
 160 are almost evenly distributed in the fluid domain (Fig. S1B in Appendix E). However, the  
 161 distribution of negative SVTs are uneven (Fig. S1A in Appendix E), with more distributed  
 162 inside the anticyclone and less distributed inside the cyclone. This is further demonstrated  
 163 in Fig. 4G, which clearly shows the large-scale vortical columns in the time averaged vortical  
 164 structure.

165 Compared with the cases at high latitudes, the sizes of LSVs at low latitudes are larger.  
 166 Since the dominant size of LSVs is in the  $x$ - $y$  plane, we expect that the vortex size follows  
 167 the relation  $\ell/h \sim [\langle v'' \rangle_{ref} / (2\Omega \sin \theta H)]^{1/2} = (Ro_c / \sin \theta)^{1/2}$  at the low Rossby regime, and  
 168 thus, the vortex size at  $\theta = 22.5^\circ$  is about 1.6 times larger than that at  $\theta = 90^\circ$ . To maintain  
 169 LSVs, the box size should be wide enough when  $\theta$  is small; otherwise, only vague vortices  
 170 or shear flows exist (the first column of Fig.3). The shear flows might be closely related to  
 171 the strong prograde and retrograde jets observed in Jupiter’s equatorial region. Near the  
 172 equatorial region,  $\theta$  is very small. Since the vortex size is proportional to  $(1/\sin \theta)^{1/2}$ , LSVs  
 173 are unlikely to be formed in the meridional-zonal plane. Alternatively, shear flows will be  
 174 favored in this region. We expect that, if the box is large enough, the critical Rossby numbers  
 175 for the appearances of LSVs would remain the same as at high latitudes. Thus we predict  
 176 that the Jovian atmosphere at low latitudes is deeper than 500km.

### 177 3. Discussion

178 Our results suggest that long-lived LSVs could be generated in a rotating deep convective  
 179 flow at both high and low latitudes, when the convective Rossby number  $Ro_c$  is smaller than  
 180 certain critical values. In particular, anticyclonic LSVs similar to the GRS can be found in  
 181 low latitudes for certain critical values of this number. Organized movements of SVTs are  
 182 responsible for the formations of LSVs. Positive SVTs are almost evenly distributed in the  
 183 whole domain. The circulation directions of LSVs are mainly determined by the unevenly  
 184 distributed negative SVTs. Tightly distributed region creates a large-scale anticyclone, while  
 185 sparsely distributed region creates a large-scale cyclone. We also found that the critical values  
 186 of  $Ro_c$  for the appearances of LSVs are insensitive to other parameters, such as the magnitude  
 187 of normalized flux and the Ekman number. This finding may have certain implication in  
 188 understanding astrophysical or geophysical flows. In stars or planets, the normalized flux and  
 189 Ekman number are usually too small to simulate directly. The convective Rossby number, a

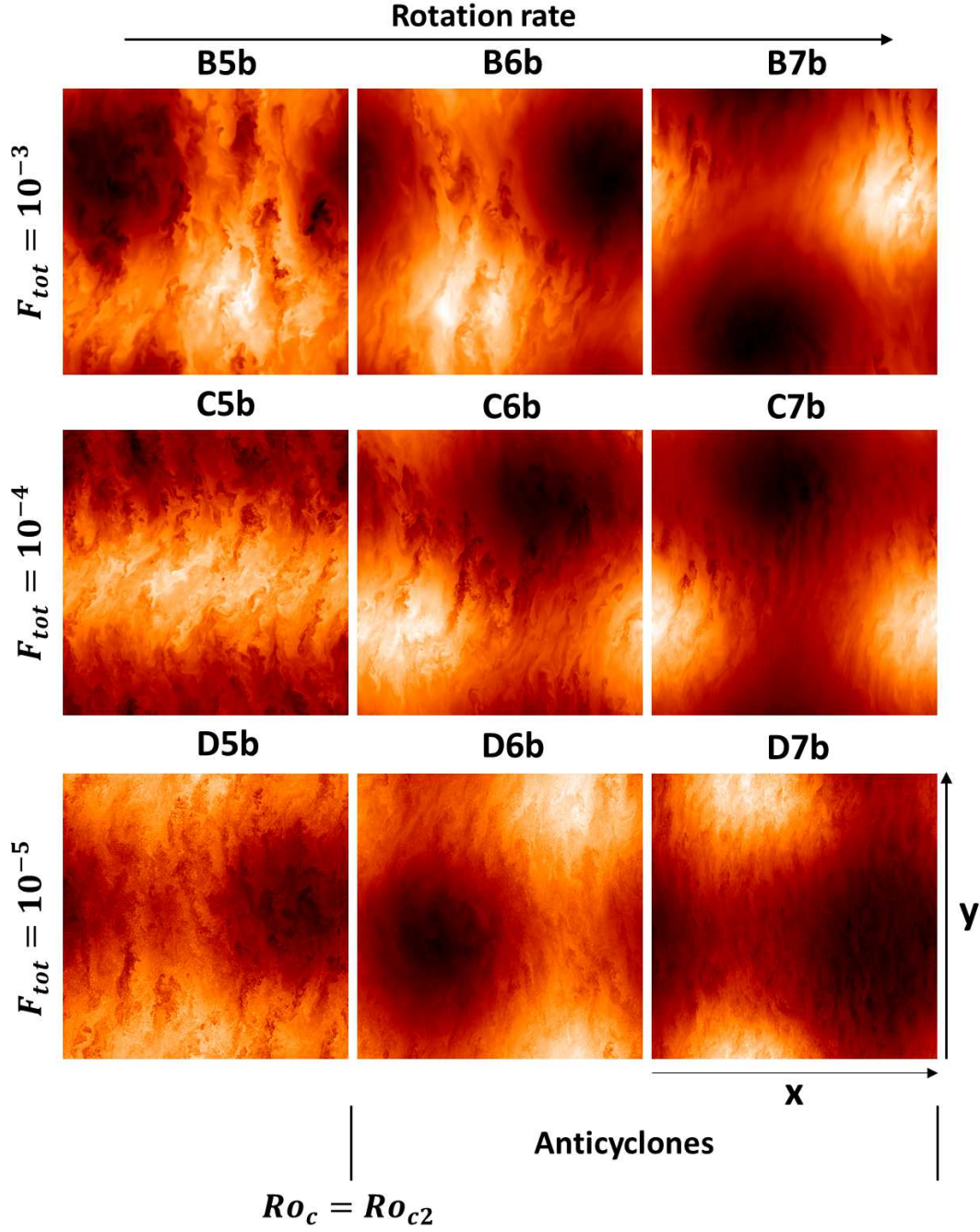


Figure 3: Flow patterns for rotating convection at the low latitude  $\theta = 22.5^\circ$ . Snapshots of the temperature perturbation taken horizontally at the mid of the convection zone  $z = 0.5$ . The rotation rate increases from left to right. Three groups with different total fluxes  $F_{tot} \in \{10^{-2}, 10^{-3}, 10^{-4}\}$  are shown from top to bottom. The settings are almost identical to B5-D7 in Fig. 1, except that the latitude is different.

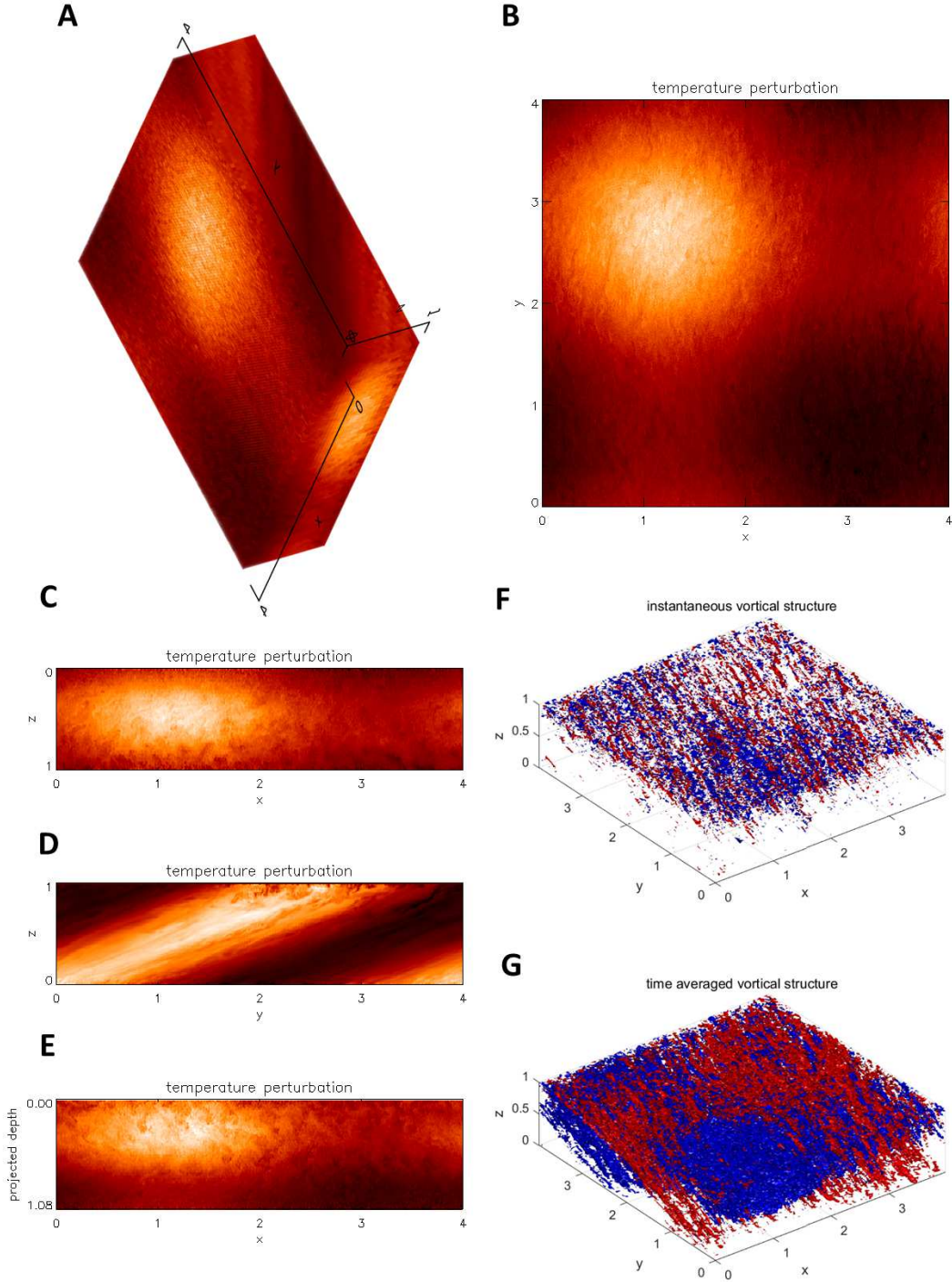


Figure 4: (A-E) Snapshots of temperature perturbation of Case D7b. (A) The 3D volume render. (B) Contours at the plane  $z = 0.1$ . (C) Contours at the plane  $y = 3.6$ . (D) Contours at the plane  $x = 3.6$ . (E) Contours at a plane perpendicular to the rotational axis. (F) The vortical structure of an instantaneous velocity field. (G) The vortical structure of time averaged (about 27 rotation periods) velocity field. Red (blue) represents positive (negative) vertical component of vorticity. The vortical structure is identified by  $\lambda_2$  criterion (see Appendix C).

viscous-free parameter, however, is not as small as the normalized flux and Ekman number, and may be reachable in numerical simulations. It can be anticipated that using similar values of convective Rossby number in the simulations of stars or planets may provide some insights on understanding the dynamics of these astrophysical or geophysical flows. For the Sun, one can estimate that  $Ro_c$  is in the range of 0.02 to 0.2. The estimation is based on the physical values that the depth of the solar convection zone  $H \approx 2.1 \times 10^8 m$ , the rotation rate  $\Omega \approx 2.6 \times 10^{-6} s^{-1}$ , and the convective velocity  $\langle v'' \rangle \approx 20 - 200 m/s$  (Miesch et al., 2008). On the basis of our calculation, we speculate that LSVs might exist at the bottom of solar convection zone, where the convective Rossby number is at around 0.02. For fast rotating solar-like stars, such as HII 296, BD-16351, and TYC 5164-567-1 (Folsom et al., 2016), the convective Rossby numbers are about 10 times smaller than that of Sun, and thus, the appearance of LSVs is very likely a prominent phenomena in these stars. One may argue that deep in the solar convection zone, the magnetic field is so strong that the formation of LSVs is inhibited by the magnetic frozen effect (Guervilly et al., 2015). This can be true in the Sun. For fast rotating solar-like stars, however, the Rossby number at the surface convective zone is already sub-critical. Thus we expect that LSVs can be formed at least in the outer part of convection zone in these stars.

Simulations at low latitudes indicate that the columnar LSVs tend to be aligned with the rotational axis, rather than the radial direction. If the GRS is formed by rotating turbulent thermal convection, we conjecture that it may also have such a columnar structure, which can extend at least 500 km deep into the atmosphere. The microwave radiometer in the Juno spacecraft can see up to 350 km deep into the GRS in Jupiter. The conjecture can be tested against the microwave radiometer data in the future.

## Acknowledgements

This work was partially supported by the Science and Technology Development Fund, Macau SAR (Nos. 0156/2019/A3, 0045/2018/AFJ), the Guangdong Basic and Applied Basic Research Foundation (No. 2019A1515011625), NSFC (No. 11503097), the China Space Agency Project (No. D020303), and the Hong Kong Research Grants Council (HKUST 600309). Part of the simulation was performed on the supercomputers at the National Supercomputer Center in Guangzhou.

## References

- [1] Li L., Ingersoll A.P., Vasavada A.R., Porco C.C., Del Genio A.D., Ewald S.P. Life cycles of spots on Jupiter from Cassini images. *Icarus*, 172, 9 (2004)
- [2] Adriani A., Mura A., Orton G., Hansen C., Altieri F., et al. Clusters of cyclones encircling Jupiter's poles. *Nature*, 555, 216 (2018)
- [3] Tabataba-Vakili F., Rogers J.H., Eichstädt G., Orton G.S., Hansen C.J., et al. Long-term tracking of circumpolar cyclones on Jupiter from polar observations with JunoCam. *Icarus*, 335, 113405 (2020)

- 228 [4] Adriani A., Bracco A., Grassi D., Moriconi M., Mura A., Orton G., et al. Two-year  
229 observations of the Jupiter polar regions by jiram on board juno. *Journal of Geophysical*  
230 *Research: Planets*, e2019JE006098 (2020)
- 231 [5] Liu J., Schneider T. Mechanisms of jet formation on the giant planets. *Journal of the*  
232 *Atmospheric Sciences*, 27, 3652 (2010)
- 233 [6] Lian Y., Showman A.P. Generation of equatorial jets by large-scale latent heating on  
234 the giant planets. *Icarus*, 207, 373 (2010)
- 235 [7] Zhang X., Showman A.P. Atmospheric circulation of brown dwarfs: Jets, vortices, and  
236 time variability. *The Astrophysical Journal Letters*, 788, L6 (2014)
- 237 [8] O’Neill M.E., Emanuel K.A., Flierl G.R. Polar vortex formation in giant-planet atmo-  
238 spheres due to moist convection. *Nature Geoscience*, 8, 523 (2015)
- 239 [9] Busse F.H. A simple model of convection in the Jovian atmosphere. *Icarus*, 29, 255  
240 (1976)
- 241 [10] Christensen U.R. Zonal flow driven by deep convection in the major planets. *Geophysical*  
242 *Research Letters*, 28, 2553 (2001)
- 243 [11] Heimpel M., Aurnou J. Turbulent convection in rapidly rotating spherical shells: A  
244 model for equatorial and high latitude jets on Jupiter and Saturn. *Icarus*, 187, 540  
245 (2007)
- 246 [12] Cai T., Chan K.L. Three-dimensional numerical simulation of convection in giant plan-  
247 ets: Effects of solid core size. *Planetary Space Science*, 71, 125 (2012)
- 248 [13] Aurnou J.M., Calkins M.A., Cheng J.S., Julien K., King E.M., et al. Rotating convective  
249 turbulence in Earth and planetary cores. *Physics of the Earth and Planetary Interiors*,  
250 246, 52 (2015)
- 251 [14] Chan K.L., Mayr H.G. Numerical simulation of convectively generated vortices: Appli-  
252 cation to the Jovian planets. *Earth and Planetary Science Letters*, 371, 212 (2013)
- 253 [15] Heimpel M., Gastine T., Wicht J. Simulation of deep-seated zonal jets and shallow  
254 vortices in gas giant atmospheres. *Nature Geosciences*, 9, 19 (2016)
- 255 [16] Cai T., Chan K.L., Mayr H.G. Deep, closely packed, long-lived cyclones on Jupiter’s  
256 poles, *The Planetary Science Journal*, 2, 81 (2021)
- 257 [17] Kaspi Y., Galanti E., Hubbard W.B., Stevenson D., Bolton S., et al. Jupiter’s atmo-  
258 sphere jet streams extend thousands of kilometers deep. *Nature*, 555, 223 (2018)
- 259 [18] Guillot T., Miquel Y., Militzer B., Hubbard W.B., Kaspi Y., et al. A suppression of  
260 differential rotation in Jupiter’s deep interior. *Nature*, 555, 227 (2018)
- 261 [19] O’Donoghue J., Moore L., Stallard T.S., Melin H., Heating of Jupiter’s upper atmosphere  
262 above the Great Red Spot. *Nature*, 536, 190 (2016)

- 263 [20] Kong D.L., Zhang K.K., Schubert G., Anderson J.D. Origin of Jupiter's cloud-level  
264 zonal winds remains a puzzle even after Juno. Proceedings of the National Academy of  
265 Sciences of the United States of America, 115, 8499 (2018)
- 266 [21] Chan K.L. Rotating convection in  $f$ -boxes: Faster rotation. Astronomical Notes, 328,  
267 1059 (2007)
- 268 [22] Käpylä P.J., Mantere M.J., Hackman T. Starspots due to large-scale vortices in rotating  
269 turbulent convection. The astrophysical Journal, 742, 34 (2011)
- 270 [23] Guervilly C., Hughes D.W., Jones C.A. Large-scale vortices in rapidly rotating Rayleigh-  
271 Bénard convection. Journal of Fluid Mechanics, 758, 407 (2015)
- 272 [24] Rubio A.M., Julien K., Knobloch E., Weiss J.B. Upscale energy transfer in three-  
273 dimensional rapidly rotating turbulent convection. Physical Review Letters, 112, 144501  
274 (2014)
- 275 [25] Favier B., Silvers L.J., Proctor M.R.E. Inverse cascade and symmetry breaking in rapidly  
276 rotating Boussinesq convection. Physics of Fluids, 26, 096605 (2014)
- 277 [26] Novi L., Hardenberg J.V., Hudhes D.W., Provenzale A., Spiegel E.A. Rapidly rotating  
278 Rayleigh-Bénard convection with a tilted axis. Physical Review E, 99, 053116 (2019)
- 279 [27] Currie L.K., Tobias S.M. Generation of shear flows and vortices in rotating anelastic  
280 convection. Physical Review Fluids, 5, 073501 (2020)
- 281 [28] Cai T. A semi-implicit spectral method for compressible convection of rotating and  
282 density-stratified flows in Cartesian geometry. Journal of Computational Physics, 310,  
283 342 (2016)
- 284 [29] Brummel N.H., Clune T.L., Toomre J. Penetration and overshooting in turbulent com-  
285 pressible convection, The Astrophysical Journal, 570, 825 (2002)
- 286 [30] Rogers T.M., Glatzmaier G.A. Penetrative convection within the anelastic approxima-  
287 tion, The Astrophysical Journal, 620, 432 (2005)
- 288 [31] Cai T. Upward overshooting in turbulent compressible convection. I. Effects of the rela-  
289 tive stability parameter, the Prandtl number, and the Péclet number. The Astrophysical  
290 Journal, 888, 46 (2020)
- 291 [32] Christensen U.R. Dynamo scaling laws and applications to the planets. Space Science  
292 Review, 152, 565 (2010)
- 293 [33] Böhm-Vitense E. über die wasserstoffkonvektionszone in sternern verschiedener effek-  
294 tivtemperaturen und leuchtkräfte. Mit 5 textabbildungen. Zeitschrift für Astrophysik,  
295 46, 108 (1958)
- 296 [34] Chan K.L. Sofia S. Turbulent compressible convection in a deep atmosphere. IV-Results  
297 of three-dimensional computations. The Astrophysical Journal, 336, 1022 (1989)

- 298 [35] Li L., Jiang X., West R., Gierasch P., Perez-Hoyos S., et al. Less absorbed solar energy  
299 and more internal heat for Jupiter. *Nature Communications*, 9, 1 (2018)
- 300 [36] Parisi M., Galanti E., Finocchiarro S., Iess L., Kaspi Y. Probing the depth of Jupiter's  
301 Great Red Spot with the Juno gravity experiment, *Icarus*, 267, 232 (2016)
- 302 [37] Sánchez-Lavega A., Hueso R., Eichstädt G., Orton G., Rogers J., Hansen C.J., et al.  
303 The rich dynamics of Jupiter's Great Red Spot from JunoCam: Juno images. *The*  
304 *Astrophysical Journal*, 156, 162 (2018)
- 305 [38] Miesch M.S., Brun A.S., DeRosa M.L., Toomre J. Structure and evolution of giant cells  
306 in global models of solar convection. *The Astrophysical Journal*, 673, 557 (2008)
- 307 [39] Folsom C.P., Petit P., Bouvier J., Lébre A., Amard L., et al. The evolution of surface  
308 magnetic fields in young solar-type stars - I. The first 250 Myr, *Monthly Notices of the*  
309 *Royal Astronomical Society*, 457, 580 (2016)
- 310 [40] Guervilly C., Hughes D.W., Jones C.A., Generation of magnetic fields by large-scale  
311 vortices in rotating convection, *Physical Review E*, 91, 041001 (2015)
- 312 [41] Cai T. Numerical analysis of nonlocal convection — Comparison with three-dimensional  
313 numerical simulations of efficient turbulent convection. *The Astrophysical Journal*, 868,  
314 1 (2018)
- 315 [42] Smagorinsky J. General circulation experiments with the primitive equations: I. The  
316 basic experiment, *Monthly Weather Review*, 91, 3 (1963)
- 317 [43] Jeong J., Hussain F. On the identification of a vortex. *Journal of Fluid Mechanics*, 285,  
318 69 (1995)
- 319 [44] Aurnou J.M., Horn S., Julien K. Connections between nonrotating, slowly rotating, and  
320 rapidly rotating turbulent convection transport scalings. *Physical Review Research*, 2,  
321 043115 (2020)

## 322 Appendix A. Numerical Method

323 For a rotating compressible flow in a Cartesian box, the hydrodynamic equations of mass,  
324 momentum, and energy conservations are

$$\partial_t \rho = -\nabla \cdot \mathbf{M} , \quad (\text{A.1})$$

$$\partial_t \mathbf{M} = -\nabla \cdot (\mathbf{M}\mathbf{M}/\rho) + \nabla \cdot \boldsymbol{\Sigma} - \nabla p + \rho \mathbf{g} - 2\boldsymbol{\Omega} \times \mathbf{M} , \quad (\text{A.2})$$

$$\partial_t E = -\nabla \cdot [(E + p)\mathbf{M}/\rho - \mathbf{M} \cdot \boldsymbol{\Sigma}/\rho + \mathbf{F}_d] + \mathbf{M} \cdot \mathbf{g} . \quad (\text{A.3})$$

325 where  $\rho$  is density,  $\mathbf{M}$  is momentum,  $\boldsymbol{\Sigma}$  is stress tensor,  $p$  is pressure,  $\mathbf{g}$  is gravity,  $\boldsymbol{\Omega}$  is angular  
326 velocity,  $E$  is total energy,  $\mathbf{F}_d$  is diffusive or conductive flux. We solve the hydrodynamic  
327 equations by a mixed finite-difference spectral model (Cai, 2016). This method has been  
328 used in the study of compressible turbulent convection (Cai, 2018) and convective overshoot-  
329 ing (Cai, 2020). In this paper, additional Coriolis term has been added in the momentum  
330 equation. In the model, all the linear terms, including the Coriolis term, are integrated semi-  
331 implicitly. An advantage of this model is that the numerical time step is not restricted by  
332 the CFL conditions associated with speeds of acoustic wave, gravity wave, or inertial wave.  
333 Thus the model is suitable for simulating rapidly rotating compressible turbulent convection  
334 at small flux. In this paper, the initial thermal structure is assumed to be in a polytropic  
335 state:

$$T/T_{top} = 1 + \eta(1 - z) , \quad (\text{A.4})$$

$$\rho/\rho_{top} = (T/T_{top})^m , \quad (\text{A.5})$$

$$p/p_{top} = (T/T_{top})^{m+1} , \quad (\text{A.6})$$

336 where  $T$  is the temperature,  $\eta$  is a ratio measuring the depth of fluid,  $m$  is the polytropic  
337 index, and the subscript *top* denotes the corresponding value at the top of the computational  
338 domain. All the physical variables are normalized by the height, density, pressure, and  
339 temperature at the top. The adiabatic polytropic index is set to be  $m_{ad} = 1.5$ . The fluid  
340 is convectively unstable when  $m < m_{ad}$ , and stable when  $m > m_{ad}$ . In our settings, we  
341 consider the rapidly rotating convection in a pure convection zone with  $\eta = 4$  and  $m = 1$ .  
342 The numerical experiments are performed with a large eddy simulation method, in which the  
343 small scale turbulence is modelled by a sub-grid-scale (SGS) turbulent model. In the SGS  
344 model (Smagorinsky, 1963), the turbulent kinematic viscosity is evaluated by

$$\nu = c_d^2 (\Delta x \Delta y)^{1/2} \Delta z (2\sigma : \sigma)^{1/2} , \quad (\text{A.7})$$

345 where  $c_d = 0.28$  is the Deardorff coefficient,  $\sigma$  is the strain rate tensor, and  $\Delta x$ ,  $\Delta y$ , and  $\Delta z$   
346 are the mesh grid sizes in the  $x$ -,  $y$ -, and  $z$ -directions, respectively. The turbulent viscosity  
347 is decomposed into two components: a time-dependent horizontal mean component and a  
348 fluctuating component. In the numerical calculations, the higher order viscous terms associ-  
349 ated with the fluctuating component are disregarded. Impenetrable and stress-free boundary  
350 conditions are used for velocities at the top and bottom of the box. The temperature is set  
351 to be a constant at the top, and a constant flux  $F_{tot} = \kappa \eta$  is supplied at the bottom. Here  
352 the thermal conductivity  $\kappa$  has a constant value throughout the domain. In the horizontal  
353 directions, periodic boundary conditions are used for all the thermodynamic variables. The

354 computational domain is a  $f$ -plane with vertical  $z$ -direction inclined to the rotational axis by  
 355 an angle  $90^\circ - \theta$ , where  $\theta$  is the latitude. The horizontal  $x$ - and  $y$ -directions of the  $f$ -plane  
 356 are corresponding to the west-to-east zonal and south-to-north meridional directions in the  
 357 spherical coordinates, respectively. Fourier spectral expansions are used in the horizontal  
 358 directions, and finite difference method is used in the vertical direction. We use density  $\rho$ ,  
 359 pressure  $p$ , total energy  $E$ , divergence of horizontal momentum  $\delta = \nabla_H \cdot \mathbf{M}_H$ , vertical com-  
 360 ponent of the curl of horizontal momentum  $\xi = \hat{z} \cdot \nabla_H \times \mathbf{M}_H$  as prognostic variables. The  
 361 components of the horizontal momentums  $\mathbf{M}_H = (M_x, M_y)$  are evaluated by linear combina-  
 362 tions of  $\delta$  and  $\xi$ . In the  $f$ -plane, additional terms on the horizontal means of  $M_x$  and  $M_y$  are  
 363 required, which can be integrated from the following equations

$$\partial_t \overline{M_x} = -\partial_z (\overline{M_x M_z / \rho}) + \partial_z (\mu \partial_z \overline{M_x / \rho}) + 2\Omega_z \overline{M_y}, \quad (\text{A.8})$$

$$\partial_t \overline{M_y} = -\partial_z (\overline{M_y M_z / \rho}) + \partial_z (\mu \partial_z \overline{M_y / \rho}) - 2\Omega_z \overline{M_x}. \quad (\text{A.9})$$

364 where  $\mu$  is the dynamic viscosity,  $\Omega_z$  is the vertical component of  $\boldsymbol{\Omega}$ , and the overline denotes  
 365 horizontal average.

366 **Appendix B. Scalings of CIA Balance**

367 For a compressible flow, the vorticity equation can be obtained by taking curl on both  
 368 sides of the moment equation:

$$\begin{aligned} \partial_t \boldsymbol{\omega} + (\mathbf{u} \cdot \nabla) \boldsymbol{\omega} - (\boldsymbol{\omega} \cdot \nabla) \mathbf{u} = \\ 2\boldsymbol{\Omega} \cdot \nabla \mathbf{u} - 2\boldsymbol{\Omega} \nabla \cdot \mathbf{u} + \nabla \times \left( \frac{1}{\rho} \nabla \cdot \boldsymbol{\Sigma} \right) - \nabla \times \left( \frac{1}{\rho} \nabla p' \right) + \nabla \times \left( \frac{\rho'}{\rho} \mathbf{g} \right), \end{aligned} \quad (\text{B.1})$$

369 where  $\mathbf{u}$  is the velocity,  $\boldsymbol{\omega} = \nabla \times \mathbf{u}$  is the vorticity,  $\boldsymbol{\Sigma}$  is the stress tensor, and  $p'$  and  $\rho'$   
 370 are perturbations from their equilibrium states. In rapidly rotating convection, **CIA** balance  
 371 among the Coriolis (**C**) term, the inertial (**I**) term, and the Archimedean (**A**) buoyancy term  
 372 is achieved in the vorticity equation (Christensen, 2010):

$$2\boldsymbol{\Omega} \cdot \nabla \mathbf{u} \sim (\mathbf{u} \cdot \nabla) \boldsymbol{\omega} \sim \nabla \times \left( \frac{\rho'}{\rho} \mathbf{g} \right). \quad (\text{B.2})$$

373 A scale analysis of the terms in the **CIA** balance gives (Aurnou et al., 2020)

$$\frac{2\Omega U}{h} \sim \frac{U^2}{\ell^2} \sim \frac{U_c^2}{\ell^2}, \quad (\text{B.3})$$

374 where  $U$  is the characteristic velocity of the LSVs,  $U_c$  is the characteristic velocity of non-  
 375 rotating convection, and  $h$  and  $\ell$  are the vertical and horizontal length scales of LSVs, re-  
 376 spectively. It quickly obtains

$$Ro_c = \frac{U_c}{2\Omega h} \sim \left( \frac{\ell}{h} \right)^2. \quad (\text{B.4})$$

377 As a result, the relative size of LSVs at small  $Ro_c$  obeys a scaling  $\ell/h \sim Ro_c^{1/2}$ . It is consistent  
 378 with the prediction of Aurnou et al. (2020), where they used the terminology system-scale  
 379 Rossby number.

## 380 Appendix C. Extraction of Vortices

381 We extract vortices by the  $\lambda_2$ -criterion (Jeong & Hussain, 1995) that the quantity  $\lambda_2$   
382 is defined as the second largest eigenvalue of the  $3 \times 3$  matrix  $A = \|\mathbf{S}^2\| + \|\boldsymbol{\omega}^2\|$ , where  
383  $\mathbf{S} = (\mathbf{J} + \mathbf{J}^T)/2$  and  $\boldsymbol{\omega} = (\mathbf{J} - \mathbf{J}^T)/2$ , and  $\mathbf{J} = \nabla \mathbf{u}$ . The vortex shape is then identified by  
384 choosing a specific negative value of  $\lambda_2$  and plotting the corresponding isosurface.

385 **Appendix D. Simulation Parameters**

386 To explore how flux affects the flow pattern in rapidly rotating flow, we performed sim-  
 387 ulations on four groups of fluxes with dimensionless values  $F_{tot} \in \{10^{-2}, 10^{-3}, 10^{-4}, 10^{-5}\}$   
 388 at latitude  $\theta = 90^\circ$ . We then choose eight different angular velocities  $\Omega$  in each group to  
 389 investigate the effect of rotation, giving a total of 32 simulation cases. The non-rotating  
 390 cases are computed for reference. The detailed parameters of each simulation case are given  
 391 in Table S1.  $F_{tot}$  is the total flux (about 80% of  $F_{tot}$  is transported by adiabatic temper-  
 392 ature gradient);  $\Omega$  is the angular velocity;  $v''$  is the root-mean-square (rms) velocity;  $v''_z$  is  
 393 the rms vertical velocity;  $v''_h$  is the rms horizontal velocity;  $Pr = \langle c_p \mu / \kappa \rangle$  is the averaged  
 394 Prandtl number;  $Re = \langle \overline{v'' H / \nu} \rangle$  is the averaged Reynolds number;  $Re_z = \langle \overline{v''_z H / \nu} \rangle$  is the  
 395 averaged vertical Reynolds number;  $Ma = \max(v/c_s)$  is the time averaged maximum Mach  
 396 number at the top layer;  $Ro_c = \langle \overline{v'' / (2\Omega H)} \rangle$  is the averaged convective Rossby number;  
 397  $E = \langle \overline{\nu / 2\Omega H^2} \rangle$  is the averaged Ekman number. The symbol  $\langle \rangle$  denotes that the average is  
 398 taken both temporarily and spatially throughout the computational domain. The symbol  
 399 overline denotes that the average is taken temporarily. The symbols ‘n’, ‘c’, and ‘ac’ denote  
 400 no LSV, large-scale cyclone, and large-scale anticyclone, respectively.

Table S1: Parameters of simulation cases of  $f$ -plane at high latitude  $\theta = 90^\circ$ 

Case	$F_{tot}$	$\Omega$	$\langle v'' \rangle$	$\langle v''_z \rangle$	$\langle v''_h \rangle$	$Pr$	$Re$	$Re_z$	$Ma$	$Ro_c$	$E$	LSV
A0	$1.0 \times 10^{-2}$	0	0.143	0.075	0.119	0.084	5036	2614	0.413	$\infty$	$\infty$	$n$
A1	$1.0 \times 10^{-2}$	0.08	0.120	0.070	0.095	0.082	4179	2425	0.384	0.891	$1.8 \times 10^{-4}$	$n$
A2	$1.0 \times 10^{-2}$	0.16	0.109	0.066	0.085	0.080	3775	2264	0.377	0.446	$9.0 \times 10^{-5}$	$n$
A3	$1.0 \times 10^{-2}$	0.32	0.103	0.062	0.081	0.079	3491	2102	0.382	0.223	$4.6 \times 10^{-5}$	$n$
A4	$1.0 \times 10^{-2}$	0.64	0.223	0.058	0.214	0.077	8301	2002	0.465	0.111	$2.3 \times 10^{-5}$	$c$
A5	$1.0 \times 10^{-2}$	1.28	0.321	0.061	0.315	0.075	12229	2141	0.699	0.056	$1.1 \times 10^{-5}$	$c$
A6	$1.0 \times 10^{-2}$	2.56	0.303	0.052	0.297	0.066	13224	2125	1.304	0.028	$4.9 \times 10^{-6}$	$ac$
A7	$1.0 \times 10^{-2}$	5.12	0.216	0.048	0.210	0.069	9102	1907	1.154	0.014	$2.5 \times 10^{-6}$	$ac$
B0	$1.0 \times 10^{-3}$	0	0.066	0.034	0.055	0.396	4703	2472	0.195	$\infty$	$\infty$	$n$
B1	$1.0 \times 10^{-3}$	0.04	0.053	0.032	0.041	0.395	3772	2299	0.186	0.825	$1.8 \times 10^{-4}$	$n$
B2	$1.0 \times 10^{-3}$	0.08	0.049	0.030	0.037	0.379	3436	2126	0.186	0.413	$8.9 \times 10^{-5}$	$n$
B3	$1.0 \times 10^{-3}$	0.16	0.045	0.028	0.035	0.373	3182	1969	0.188	0.206	$4.5 \times 10^{-5}$	$n$
B4	$1.0 \times 10^{-3}$	0.32	0.089	0.026	0.085	0.367	6822	1848	0.217	0.103	$2.2 \times 10^{-5}$	$c$
B5	$1.0 \times 10^{-3}$	0.64	0.149	0.025	0.146	0.354	11999	1845	0.274	0.052	$1.1 \times 10^{-5}$	$c$
B6	$1.0 \times 10^{-3}$	1.28	0.205	0.027	0.203	0.342	17196	2090	0.547	0.026	$5.3 \times 10^{-6}$	$c+ac$
B7	$1.0 \times 10^{-3}$	2.56	0.144	0.025	0.142	0.341	12069	1918	0.707	0.013	$2.6 \times 10^{-6}$	$c+ac$
C0	$1.0 \times 10^{-4}$	0	0.030	0.016	0.025	1.844	4556	2430	0.091	$\infty$	$\infty$	$n$
C1	$1.0 \times 10^{-4}$	0.02	0.024	0.015	0.019	1.792	3594	2215	0.087	0.756	$1.7 \times 10^{-4}$	$n$
C2	$1.0 \times 10^{-4}$	0.04	0.022	0.014	0.017	1.760	3259	2046	0.087	0.378	$8.4 \times 10^{-5}$	$n$
C3	$1.0 \times 10^{-4}$	0.08	0.020	0.013	0.016	1.739	3004	1879	0.087	0.189	$4.2 \times 10^{-5}$	$n$
C4	$1.0 \times 10^{-4}$	0.16	0.035	0.012	0.033	1.726	5681	1730	0.101	0.095	$2.1 \times 10^{-5}$	$c$
C5	$1.0 \times 10^{-4}$	0.32	0.056	0.011	0.055	1.711	9190	1626	0.114	0.047	$1.1 \times 10^{-5}$	$c$
C6	$1.0 \times 10^{-4}$	0.64	0.102	0.011	0.102	1.780	16330	1620	0.183	0.023	$5.5 \times 10^{-6}$	$c+ac$
C7	$1.0 \times 10^{-4}$	1.28	0.062	0.099	0.061	1.743	9954	1464	0.246	0.012	$2.7 \times 10^{-6}$	$c+ac$
D0	$1.0 \times 10^{-5}$	0	0.014	0.007	0.011	8.617	4399	2350	0.043	$\infty$	$\infty$	$n$
D1	$1.0 \times 10^{-5}$	0.01	0.011	0.007	0.008	8.371	3421	2127	0.040	0.686	$1.6 \times 10^{-4}$	$n$
D2	$1.0 \times 10^{-5}$	0.02	0.098	0.006	0.008	8.252	3102	1952	0.040	0.343	$8.0 \times 10^{-5}$	$n$
D3	$1.0 \times 10^{-5}$	0.04	0.009	0.006	0.007	8.170	2845	1786	0.040	0.171	$4.0 \times 10^{-5}$	$n$
D4	$1.0 \times 10^{-5}$	0.08	0.017	0.005	0.016	8.131	5577	1597	0.049	0.086	$2.0 \times 10^{-5}$	$c$
D5	$1.0 \times 10^{-5}$	0.16	0.026	0.005	0.025	8.045	8998	1444	0.057	0.043	$1.0 \times 10^{-5}$	$c$
D6	$1.0 \times 10^{-5}$	0.32	0.028	0.004	0.027	8.166	9529	1216	0.059	0.021	$5.1 \times 10^{-6}$	$c+ac$
D7	$1.0 \times 10^{-5}$	0.64	0.013	0.003	0.012	8.103	4360	904	0.057	0.011	$2.5 \times 10^{-6}$	$ac$

401 To investigate whether LSVs could be formed at low latitudes, we performed a total of  
402 9 simulations with different fluxes and angular velocities in the tilted  $f$ -plane at the latitude  
403  $\theta = 22.5^\circ$ . The basic settings of B5b-B7b, C5b-C7b, and D5b-D7b are all the same to the  
404 simulation Cases B5-B7, C5-C7, and D5-D7 at the latitude  $\theta = 90^\circ$ . The only difference is  
405 that the angular velocity has two components in the tilted  $f$ -plane: the vertical component  
406  $\Omega \sin \theta$  along the  $z$ -direction, and the horizontal component  $\Omega \cos \theta$  along the  $y$ -direction. The  
407 symbol ‘ $s$ ’ in the last column denotes shear flow. The detailed parameters of each simulation  
408 case are given in Table S2. Other parameters and symbols have the same meanings as  
409 mentioned in Table S1.

Table S2: Parameters of simulation cases of  $f$ -plane at low latitude  $\theta = 22.5^\circ$

Case	$F_{tot}$	$\Omega$	$\langle v'' \rangle$	$\langle v''_z \rangle$	$\langle v''_h \rangle$	$Pr$	$Re$	$Re_z$	$Ma$	$Ro_c$	$E$	LSV
B5b	$1.0 \times 10^{-3}$	0.64	0.086	0.025	0.082	0.343	6905	1945	0.275	0.052	$1.0 \times 10^{-5}$	$c$
B6b	$1.0 \times 10^{-3}$	1.28	0.113	0.023	0.110	0.335	9491	1844	0.342	0.026	$5.0 \times 10^{-6}$	$c+ac$
B7b	$1.0 \times 10^{-3}$	2.56	0.111	0.021	0.109	0.336	9439	1712	0.375	0.013	$2.5 \times 10^{-6}$	$c+ac$
C5b	$1.0 \times 10^{-4}$	0.32	0.030	0.012	0.028	1.672	4880	1870	0.118	0.047	$1.0 \times 10^{-6}$	$s$
C6b	$1.0 \times 10^{-4}$	0.64	0.046	0.011	0.045	1.663	7753	1743	0.156	0.023	$5.0 \times 10^{-6}$	$c+ac$
C7b	$1.0 \times 10^{-4}$	1.28	0.045	0.089	0.044	1.568	8810	1530	0.173	0.012	$2.4 \times 10^{-6}$	$c+ac$
D5b	$1.0 \times 10^{-5}$	0.16	0.017	0.005	0.017	7.984	5939	1726	0.059	0.043	$9.8 \times 10^{-6}$	$c$
D6b	$1.0 \times 10^{-5}$	0.32	0.023	0.004	0.023	7.765	8398	1499	0.066	0.022	$4.8 \times 10^{-6}$	$c+ac$
D7b	$1.0 \times 10^{-5}$	0.64	0.015	0.004	0.014	7.657	5317	1335	0.061	0.011	$2.4 \times 10^{-6}$	$c+ac$

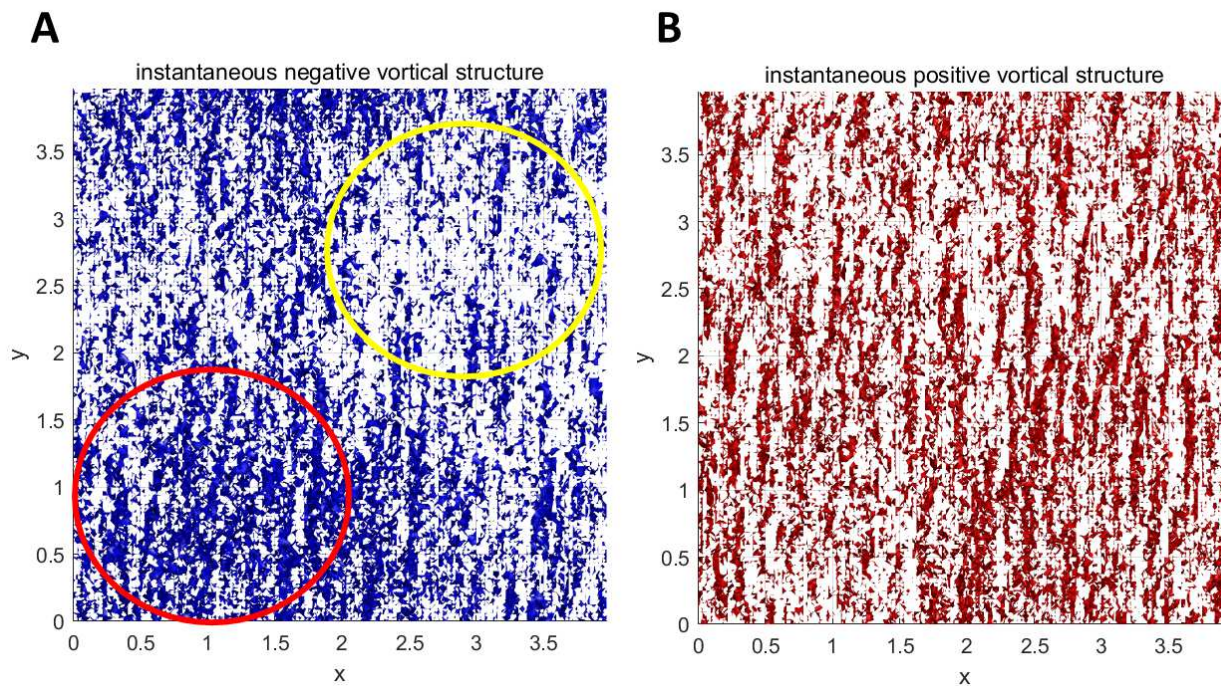


Figure S1: Vortical structures of Case D7b viewed from the above. (A) The vortical structure with negative vertical vorticity. The red circle shows the location of large-scale anticyclone, and the yellow circle shows the location of large-scale cyclone. (B) The vortical structure with positive vertical vorticity.

## 411 **Appendix F. Movies**

412 Movie S1. Time evolution of temperature perturbation at  $z = 0.1$  of Case D7b. The  
413 time period is about 27 rotation periods. The bright (dark) color denotes higher (lower)  
414 temperature.

415  
416 Movie S2. Time evolution of temperature perturbation at  $z = 0.9$  of Case D7b. The  
417 time period is about 27 rotation periods. The bright (dark) color denotes higher (lower)  
418 temperature.

419  
420 Movie S3. Time evolution of temperature perturbation at  $y = 3.6$  of Case D7b. The  
421 time period is about 27 rotation periods. The bright (dark) color denotes higher (lower)  
422 temperature.

423  
424 Movie S4. Time evolution of temperature perturbation at  $x = 3.6$  of Case D7b. The  
425 time period is about 27 rotation periods. The bright (dark) color denotes higher (lower)  
426 temperature.

427  
428 Movie S5. Time evolution of vortical structure with positive (red color) and negative  
429 (blue color) vertical vorticity of Case D7b. The time period is about 27 rotation periods.

## Supplementary Files

This is a list of supplementary files associated with this preprint. Click to download.

- [MovieS1.mpg](#)
- [MovieS2.mpg](#)
- [MovieS3.mpg](#)
- [MovieS4.mpg](#)
- [MovieS5.mpg](#)